The effect of Schmidt number on gravity current flows: The formation of large-scale three-dimensional structures

Cite as: Phys. Fluids **33**, 106601 (2021); https://doi.org/10.1063/5.0064386
Submitted: 22 July 2021 • Accepted: 02 September 2021 • Published Online: 05 October 2021

C. R. Marshall, R. M. Dorrell, S. Dutta, et al.

Physics of Fluids ARTICLE scitation.org/journal/phf

The effect of Schmidt number on gravity current flows: The formation of large-scale three-dimensional structures

Cite as: Phys. Fluids 33, 106601 (2021); doi: 10.1063/5.0064386
Submitted: 22 July 2021 · Accepted: 2 September 2021 ·
Published Online: 5 October 2021

View Online Export Citation CrossMark

C. R. Marshall,[1,a)] R. M. Dorrell,[2] S. Dutta,[3] G. M. Keevil,[4] J. Peakall,[4] and S. M. Tobias[5]

AFFILIATIONS

[1]EPSRC Centre for Doctoral Training in Fluid Dynamics, University of Leeds, Leeds LS2 9JT, United Kingdom
[2]Institute of Energy and Environment, University of Hull, Hull HU6 7RX, United Kingdom
[3]Mechanical and Aerospace Engineering, Utah State University, Logan, Utah 84322, USA
[4]School of Earth and Environment, University of Leeds, Leeds LS2 9JT, United Kingdom
[5]School of Mathematics, University of Leeds, Leeds LS2 9JT, United Kingdom

[a)]Author to whom correspondence should be addressed: matcm@leeds.ac.uk

ABSTRACT

The Schmidt number, defined as the ratio of scalar to momentum diffusivity, varies by multiple orders of magnitude in real-world flows, with large differences in scalar diffusivity between temperature, solute, and sediment driven flows. This is especially crucial in gravity currents, where the flow dynamics may be driven by differences in temperature, solute, or sediment, and yet the effect of Schmidt number on the structure and dynamics of gravity currents is poorly understood. Existing numerical work has typically assumed a Schmidt number near unity, despite the impact of Schmidt number on the development of fine-scale flow structure. The few numerical investigations considering high Schmidt number gravity currents have relied heavily on two-dimensional simulations when discussing Schmidt number effects, leaving the effect of high Schmidt number on three-dimensional flow features unknown. In this paper, three-dimensional direct numerical simulations of constant-influx solute-based gravity currents with Reynolds numbers $100 \leq Re \leq 3000$ and Schmidt number 1 are presented, with the effect of Schmidt number considered in cases with $(Re, Sc) = (100, 10)$, $(100, 100)$, and $(500, 10)$. These data are used to establish the effect of Schmidt number on different properties of gravity currents, such as density distribution and interface stability. It is shown that increasing Schmidt number from 1 leads to substantial structural changes not seen with increased Reynolds number in the range considered here. Recommendations are made regarding lower Schmidt number assumptions, usually made to reduce computational cost.

I. BACKGROUND

Gravity currents are primarily horizontal flows arising from a density difference between the current and surrounding ambient fluids. This density difference occurs with variation in concentration of solutes or suspended sediments or temperature difference between the current and the ambient fluids.[1,2] Gravity currents are a common class of flow, with examples including thunderstorm outflows and powder snow avalanches,[1,3] and are one of the primary mechanisms of sediment transport in oceans.[4,5] There exists extensive research into the dynamics of gravity currents, including numerical investigations.[6–13] The typical structure of gravity current flows as described by Kneller and Buckee[14] is presented in Fig. 1 and consists of a head region followed by a body. This body can be divided into a dense lower layer overlaid by a less-dense layer of mixed current and ambient fluids. Despite the body typically forming by far the largest part of gravity current flows,[15–17] the existing research has primarily focused on the head of the flow. Additionally, numerical work has typically assumed a Schmidt number of 1 to investigate flows with $Sc = \mathcal{O}(1000)$.[6,9,11–13,18–24] Therefore, characteristics such as the effect of Schmidt number on the flow, and the nature of large-scale structures within the body, remain poorly understood.

Gravity current properties are characterized using a small number of dimensionless parameters:[14] the Reynolds, densimetric Froude (affected by the bed slope[26]), gradient Richardson, and Schmidt numbers. The Reynolds number is defined as the ratio of inertia to viscous forces ($Re = \frac{U_c L_c}{\nu}$, where U_c and L_c are velocity and length scales that

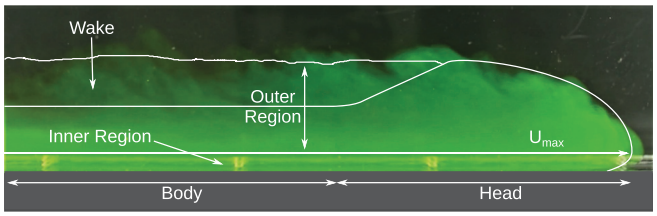

FIG. 1. Flow visualization from the work presented in Marshall *et al.*,[25] overlaid by a gravity current structure as described by Kneller and Buckee.[14]

are characteristic of the flow, and ν is the kinematic viscosity of the fluid), and increasing Reynolds number reduces the size of the smallest length scales within the flow that must be resolved while conducting direct numerical simulations (DNS).[27] Decreasing Reynolds number, below the point of similarity ($Re \approx 1000$),[1] also changes the nature of the current head including the formation of Kelvin–Helmholtz billows and the over-riding of ambient fluid leading to lobe-and-cleft structures.[1,28,29] *Re* significantly affects rates of mixing and entrainment, with increasing *Re* dictating whether the primary mixing mechanism is Holmboe waves, Kelvin–Helmholtz vortex rolls, or Kelvin–Helmholtz billows.[30,31] The Schmidt number, analogous to the Prandtl number, is defined as the ratio of momentum and mass diffusivities ($Sc = \nu/D$, where D is mass diffusivity) and is a key parameter in understanding mixing on the molecular level.[32,33] As Schmidt number increases, diffusion decreases and momentum becomes the dominant mass transfer mechanism.

Increasing the Schmidt number from 1 reduces the length scales associated with mixing within the flow, reducing the smallest lengths that must be captured from the Kolmogorov scale (η_K) to the Batchelor scale ($\eta_B = \eta_K Sc^{-1/2}$),[34,35] and mixing is expected to decrease.[32,36] It has been demonstrated that the finer-scale structures that develop with increasing Schmidt number may cause larger scale structural changes in the flow, such as increased plume length in turbulent jets,[32] and stronger three-dimensional motions resulting from changes to density profiles and stronger density gradients.[36–38]

The value of Schmidt number varies dramatically depending on the source of the density difference, for example being $\mathcal{O}(1)$ for temperature-driven flows, $\mathcal{O}(1000)$ for solutes in water, and being strongly dependent on grain size but often much larger for sediment in water [for example, being $\mathcal{O}(10^9)$ for 100 μm sand].[8,33,34,39–41] Despite this, existing numerical investigations into gravity current structure typically assume $Sc = 1$.[6–10,33,42,43] The large computational cost involved in resolving the Batchelor scale (the cost of direct numerical simulation scaling with Re^3Sc^2)[27,34] means that few works have so far considered the effect of Schmidt number on gravity current flows. Birman *et al.*[42] and Necker *et al.*[43] justify their use of $Sc = 1$ through test calculations that suggest Schmidt number has little influence on gravity current structure for $Sc = 0.2 \rightarrow 5$, while Härtel *et al.*[44] claim that Schmidt number dependence is weak unless *Sc* is very small ($\ll 1$). Ooi *et al.*[45] use comparison of two two-dimensional large-eddy simulations of lock-exchange type flows, with a similar comparison of two three-dimensional large-eddy simulations in Ooi *et al.*,[46] to conclude that Schmidt number has only a small effect on properties such as current front velocity and shape. The effect of Schmidt number on other flow features is not considered, nor the combined effects of Reynolds and Schmidt number. Deepwell and Stastna,[47] in their study of flows consisting of a gravity current traveling along a pycnocline(s), conclude that the mass transport capability of internal solitary-like waves increases as Schmidt number is increased between 1 and 20, but does not continue to change when Schmidt number is further increased to 40 (suggesting that exact Schmidt number matching may not be required to capture flow dynamics). To date, the only research including a parametric study investigating the effect of Schmidt number on gravity current flows is the work of Bonometti and Balachandar.[33]

Bonometti and Balachandar[33] use a combination of a pseudo-spectral method and a finite-volume/volume of fluid interface capturing method to investigate the parameter space $1 \leq Sc \leq \infty$ and $100 \leq Re \leq 10\,000$. For $Re = 10\,000$, they conclude that neither the front velocity nor the level of mixing is strongly dependent on *Sc*, though decreasing *Sc* does increase the thickness of the layer of mixed ambient and current fluids. For the lower Reynolds number flows, they observe that increasing *Sc* changes head shape, with a depression separating head from body appearing as *Sc* increases, and that the effect of *Sc* on front velocity in these flows is highly dependent on the density contour chosen to define the front. They also claim that while the pattern of lobe-and-cleft structures is not strongly dependent on the Schmidt number, the formation of vortices along the body is. A scatterplot based on a table from Bonometti and Balachandar[33] is presented in Fig. 2, showing the distribution of stable/unstable interfaces between the current and ambient fluids based on a bulk Richardson number for their work and a few other investigations. This suggests that the interface stability is only weakly dependent on Schmidt number, with the interface becoming slightly more stable with increased *Sc*. However, these data are based almost entirely on two-dimensional direct numerical simulation (DNS) datasets. The flow structure resulting from two- and three-dimensional simulation of gravity currents with Reynolds numbers 317 and 10^4 from the work of Bonometti and Balachandar[33] is presented in Fig. 3. While the two-dimensional work captures some features well, others require consideration of three-dimensional flow. Two-dimensional DNS of gravity currents is not able to reproduce large-scale coherent motions and three-dimensional flow features, such as the formation of lobe-and-cleft structures and the breakdown of interfacial billows, capture the spanwise dissipation of energy, or accurately estimate the energy budget of the flow.[8,9,20,22,48–50] Therefore, three-dimensional simulations are needed to establish the effect of Schmidt number on three-dimensional flow

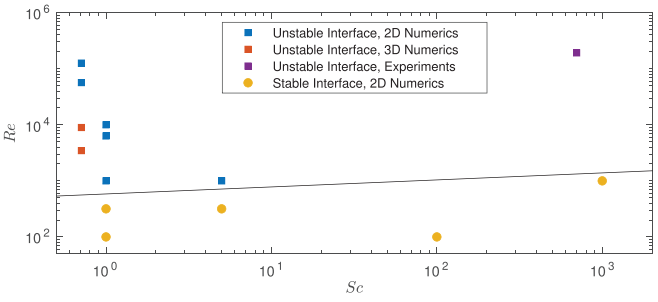

FIG. 2. Scatterplot showing the distribution of stable/unstable interfaces based on a bulk Richardson number as a function of *Sc* and *Re*. Data from the work of Bonometti and Balachandar.[33]

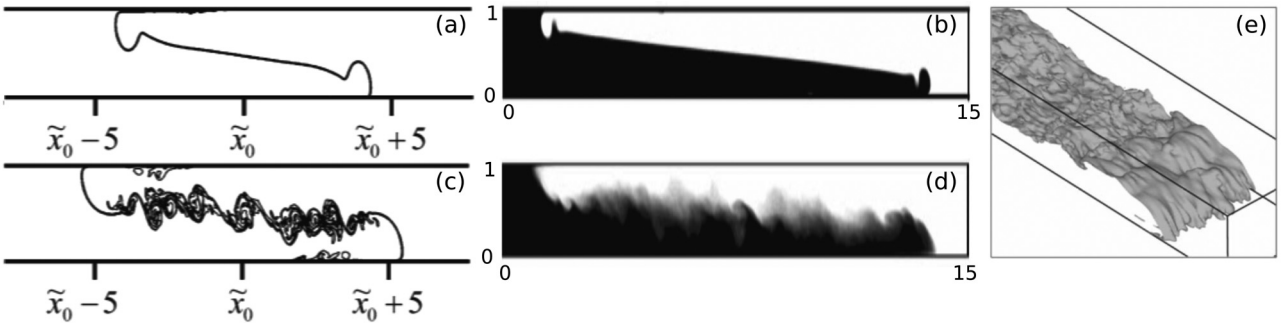

FIG. 3. Contours of density from (a) and (c) two- and (b), (d), and (e) three-dimensional simulation of gravity current flows with (a) and (b) $Re = 317$ and (c)–(e) $Re = 10^4$ from Bonometti and Balachandar.[33] (b) and (d) show spanwise averaged data from three-dimensional investigations. Reproduced with permission from T. Bonometti and S. Balachandar, Theor. Comput. Fluid Dyn. **22**, 341 (2008). Copyright 2008 Springer-Verlag.

features and to confirm the relationship between interface stability and Schmidt number.

In this work, three-dimensional direct numerical simulation (DNS) is used to investigate the structure and dynamics of constant-influx solute-based gravity current flows by providing the instantaneous density and velocity fields. As well as considering the effect of Reynolds number, the impact of varying the Schmidt number on both the head and body of gravity current flows will be investigated. The work addresses some of the remaining questions regarding how reasonable an assumption of $Sc = 1$ is for such flows, specifically the key aims are to discuss: (i) how Reynolds and Schmidt numbers affect the structure of the head, in particular, the formation of lobe-and-cleft structures, (ii) how Reynolds and Schmidt numbers affect the structure of flow behind the head, in particular, the stability of the current–ambient interface, (iii) which of the changes observed with increased Schmidt number also occur with increased Reynolds number, and (iv) when assuming a low Schmidt number to reduce the computational cost of numerical investigations may be justified.

II. METHODOLOGY

The spectral element solver Nek5000[51] is used to simulate three-dimensional gravity current in the domain illustrated in Fig. 4. This domain is designed to closely reproduce the experimental domain presented in Marshall *et al.*,[25] Marshall,[52] with a simplified outlet. The governing equations are the nondimensional, incompressible, Boussinesq Navier–Stokes, salinity, and continuity equations,

$$\begin{aligned} \frac{\partial \tilde{\boldsymbol{U}}}{\partial \tilde{t}} + \tilde{\boldsymbol{U}} \cdot \nabla \tilde{\boldsymbol{U}} &= -\nabla \tilde{P} + \frac{1}{Re} \nabla . \tilde{\tau} + \frac{1}{Fr_d^2} \Delta \tilde{S} \hat{\boldsymbol{g}}, \\ \frac{\partial \tilde{S}}{\partial \tilde{t}} + \tilde{\boldsymbol{U}} \cdot \nabla \tilde{S} &= \frac{1}{ReSc} \nabla \cdot \nabla \tilde{S}, \\ \nabla \cdot \tilde{\boldsymbol{U}} &= 0, \end{aligned} \tag{1}$$

where $\boldsymbol{U}$ is the velocity vector, t time, $P = p + \rho_a g Y$ where P is the kinematic pressure field, τ the stress tensor, $Re = U_c L_c / \nu$ the Reynolds number, ν the kinematic viscosity, $Fr_d = U_c / \sqrt{g' L_c}$ the densimetric Froude number, $Sc = \nu / D$ the Schmidt number, D the mass diffusivity, g and $\hat{\boldsymbol{g}} = (\sin\theta, \cos\theta, 0)$ the magnitude and direction of the gravitational acceleration, θ bed slope, S salinity [with $\Delta S = (S - S_a)$], $(\cdot)_a$ indicates a property of the ambient fluid, and $\tilde{(\cdot)}$ indicates a dimensionless variable. As described in McWilliams,[53] here a simplified linear dependence of density on salinity has been employed,

$$\rho \approx \rho_a (1 + \beta \Delta S), \tag{2}$$

where ρ is density, and $\beta = \frac{1}{\rho} \frac{\partial \rho}{\partial S}$ the haline contraction coefficient. The dimensionless variables are defined relative to the characteristic length, velocity, and time scales as shown in Table I. Time advancement is

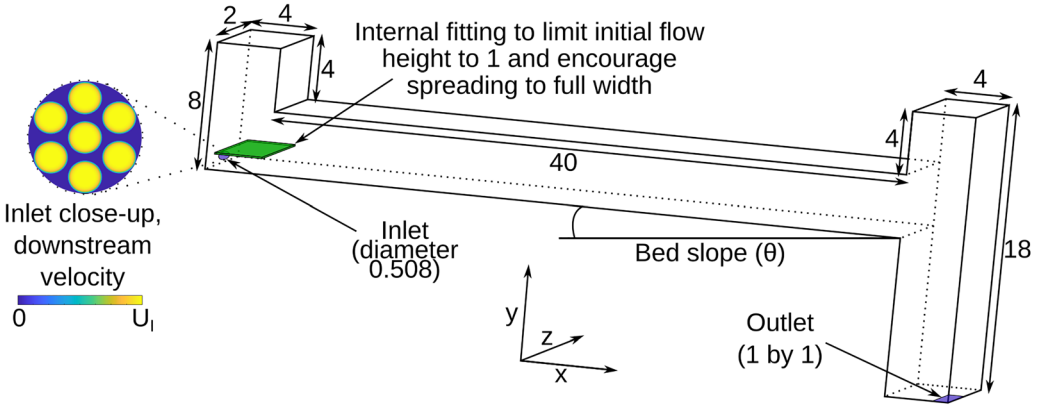

FIG. 4. The experimental setup of Marshall *et al.*,[25] Marshall,[52] used to investigate the structure of the gravity current body, here used to define the DNS domain.

TABLE I. Definition of nondimensionalizations used in this work, where X is position, t is time, $t_c = L_c/U_c$ a characteristic time, $\Delta S = S - S_a$, and $\Delta S_I = S_I - S_a$.

Parameter	Nondimensionalization
Length	$\tilde{X} = X/L_c$
Velocity	$\tilde{\boldsymbol{U}} = \boldsymbol{U}/U_c$
Time	$\tilde{t} = (U_c/L_c)t = t/t_c$
Pressure	$\nabla \tilde{P} = (L_c/\rho_a U_c^2)\nabla P$
Stress tensor	$\nabla \cdot \tilde{\tau} = (L_c^2/U_c \nu \rho_a)\nabla \cdot \tau$
Salinity	$\Delta \tilde{S} = (S - S_a)/(S_I - S_a) = \Delta S/\Delta S_I$

performed using a semi-implicit scheme that combines the implicit third-order backward difference and the explicit third-order extrapolation schemes, as described in Mittal *et al.*[54] Spatial discretization is based on the high-order spectral element method.[55–57] To ensure sufficient resolution, the wall y^+, x^+, and z^+ values (defined as $y^+ = u_w y/\nu$ where y is the distance to the nearest wall, and u_w the wall friction velocity with equivalent statements for the other spatial dimensions) are kept below 0.05 for the nearest grid point to the wall, and the first ten points are within $y^+ < 10$.[58,59] Additionally, decay of several orders of magnitude is observed in the energy spectrum for all variables.[6,60]

The characteristic length L_c, velocity U_c, and time t_c scales are defined *a priori*. The characteristic length scale for all cases is chosen to be the height of the internal fitting to limit initial flow height, $L_c = 0.05$ m (refer to Fig. 4). For the highest Reynolds number case, the viscosity is chosen to match that of the experimental work in Marshall *et al.*,[25] Marshall,[52] $\nu = 1.09 \times 10^{-6}\ \mathrm{m^2\,s^{-1}}$, and the characteristic velocity, $U_c = 0.065\ \mathrm{ms^{-1}}$, is chosen to give the desired input Reynolds number $Re_I = 3000$. This represents an average velocity under the initial internal fitting. The characteristic timescale $T_c = L_c/U_c = 0.77\ s$. To reduce the Reynolds number, the characteristic velocity scale is kept constant and the fluid viscosity varied. Schmidt number is varied by changing mass diffusivity, D. The input densimetric Froude number, $Fr_{D,I} = U_c/\sqrt{g' L_c} = 0.54$, is the same for all cases, as is the source Froude number calculated using the inlet velocity ($U_I = 0.22\ \mathrm{ms^{-1}}$) and inlet diameter ($L_I = 0.0254\ m$) as characteristic velocity and length scales, $Fr_{D,S} = U_I/\sqrt{g' L_I} = 2.54$. The input parameters for each case are shown in Table II.

The inlet flow is matched to Marshall *et al.*[25] and Marshall.[52] The maximum inlet velocity in this work, U_I, is approximated by dividing the lowest influx value from Marshall *et al.*[25] ($7 \times 10^{-5}\ \mathrm{m^3\,s^{-1}}$) by the inlet area ($3.34 \times 10^{-4}\ \mathrm{m^2}$). The inlet has a dimensionless radius of 0.254 and is covered with a coarse mesh with holes of dimensionless radius 0.078. These holes are centered at locations,

$$(\tilde{Y}, \tilde{Z}) = (0.350,\ 1.000), (0.531,\ 1.000), (0.169,\ 1.000), (0.441,\ 1.150), (0.260,\ 1.150), (0.441,\ 0.850), (0.260,\ 0.850), \quad (3)$$

with the inlet velocity approximated by

$$\tilde{U} = \tilde{U}_I \sqrt{\sin\left((0.5 + 0.5r^2)\pi\right)}, \quad (4)$$

where r varies from 0 to 1 from the center to the edge of each small circle. Where the velocity on the inlet is nonzero the salinity $\tilde{S} = 1.03$, compared to $\tilde{S} = 1.00$ in the rest of the domain, and therefore $\Delta S_I = 0.03$ with a haline contraction coefficient of $\beta = 1$ to achieve a density difference of 3% between the current and ambient fluids. The outlet is approximated by a square outlet placed in the bottom right corner of the domain, with a special boundary condition implementation that matches the total outflow to the net inflow into the domain. In this work, X, Y, and Z correspond to downstream, vertical, and cross-stream directions with corresponding downstream, vertical, and cross-stream velocities U, V, and W.

III. THE EFFECT OF REYNOLDS AND SCHMIDT NUMBERS

A. Density

The effect of Schmidt number on the density structure of the flow can be established by considering contours of proportional excess density ($\Delta\tilde{S}$). Figure 5 shows contours of $\Delta\tilde{S}$ at $\tilde{t} = 23.4$ at a central cross-stream location. The rightmost column of this figure shows two contours for each case—that with density just above the ambient density, $\Delta\tilde{S} = 0.03$, and that with density halfway between the densities of the ambient fluid and that pumped in at the inlet, $\Delta\tilde{S} = 0.48$. The contour with $\Delta\tilde{S} = 0.03$ is considered to be the current boundary. Increasing Schmidt number has little impact on current front velocity over the short time frame considered here, though increasing Reynolds number increases front velocity as expected. Increasing either Reynolds number or Schmidt number leads to a depression behind the head, angled toward the current front.

For each case, the current height (defined as the height of the $\Delta\tilde{S} = 0.03$ contour at the left-most point in Fig. 5), the thickness of the mixed region (defined as the difference in height of the $\Delta\tilde{S} = 0.03$ and $\Delta\tilde{S} = 0.48$ contours at the left-most point of the figure), and the difference in front positions of the $\Delta\tilde{S} = 0.03$ and $\Delta\tilde{S} = 0.48$

TABLE II. Parameters for the various simulations conducted in this work, along with a bed slope of $\theta = 0.1°$, and a haline contraction coefficient of $\beta = 1$ and $S_I - S_a = 0.03$ to achieve a 3% density difference.

Re_I	Sc	Pe	L_c (m)	ν ($\mathrm{m^2\,s^{-1}}$)	U_c ($\mathrm{m\,s^{-1}}$)	$Fr_{D,I}$	U_I ($\mathrm{m\,s^{-1}}$)	t_c (s)	D ($\mathrm{m^2\,s^{-1}}$)
100	1	100	0.05	3.26×10^{-5}	0.065	0.54	0.22	0.77	3.26×10^{-5}
100	10	1000	0.05	3.26×10^{-5}	0.065	0.54	0.22	0.77	3.26×10^{-6}
100	100	10 000	0.05	3.26×10^{-5}	0.065	0.54	0.22	0.77	3.26×10^{-7}
500	1	500	0.05	6.53×10^{-6}	0.065	0.54	0.22	0.77	6.53×10^{-6}
500	10	5000	0.05	6.53×10^{-6}	0.065	0.54	0.22	0.77	6.53×10^{-7}
1000	1	1000	0.05	3.26×10^{-6}	0.065	0.54	0.22	0.77	3.26×10^{-6}
3000	1	3000	0.05	1.09×10^{-6}	0.065	0.54	0.22	0.77	1.09×10^{-6}

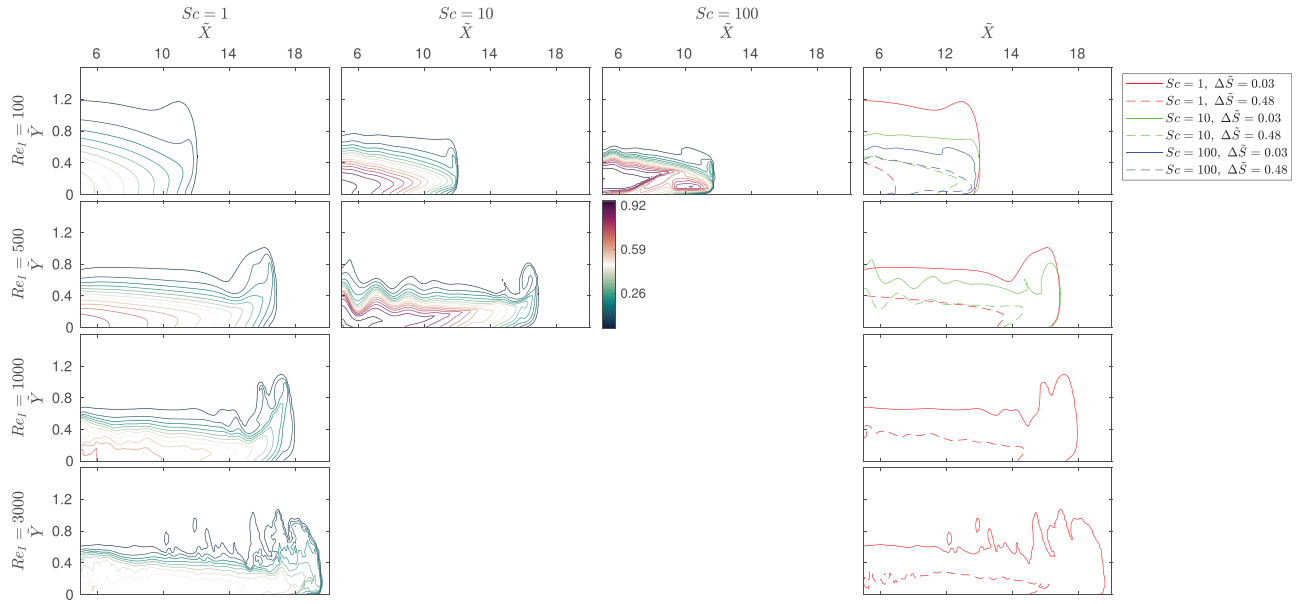

FIG. 5. Contours of $\Delta\tilde{S}$ on a central cross-stream slice within the domain at $\tilde{t} = 23.4$. From top to bottom, the inlet Reynolds number $Re_I = 100,\ 500,\ 1000,\ 3000$ and from left to right $Sc = 1,\ 10,\ 100$ with the rightmost column showing density contours at $\Delta\tilde{S} = 0.03$ and $\Delta\tilde{S} = 0.48$ for each case.

contours are estimated by inspecting Fig. 5, and listed in Table III. The height of the head is approximately constant across cases with constant Schmidt number. For $Sc = 1$ the head height is $\tilde{Y} \approx 1.1$, reducing to $\tilde{Y} \approx 0.8$ for $Sc = 10$. Increasing Schmidt number consistently reduces body height, the thickness of the mixed layer as a proportion of total flow height (Fig. 6), and the difference in the front position of the two contours (illustrating that increasing Schmidt number leads to dense fluid reaching closer to the front of the flow).

The height of the $\Delta\tilde{S} = 0.48$ contour, however, is not strongly affected by increasing Schmidt number, suggesting that evidence of the effect of Schmidt number on quantities such as current height or front velocity is highly dependent on the contour chosen to define the current boundary. In fact, the height of this contour is the same across all cases except $Re_I = 3000$, suggesting a greater degree of mixing in this case. This is likely an artifact of relatively short simulation duration. Longer simulation time will result in changes in contours further from the interface. Increasing Schmidt number reduces current height, with a 33% decrease between the $(Re_I, Sc) = (100, 1)$ and $(100, 10)$ cases [with a further decrease of 25% between $(Re_I, Sc) = (100, 10)$ and $(100, 100)$], though this decrease is reduced to 25% between $(Re_I, Sc) = (500, 1)$ and $(500, 10)$. Similarly increasing Schmidt number reduces the percentage of the current height taken up by the mixed layer, from 67% to 38% between the $(Re_I, Sc) = (100, 1)$ and $(100, 10)$ cases [to only 17% in the $(Re_I, Sc) = (100, 100)$ case], and from 50% to 33% between $(Re_I, Sc) = (500, 1)$ and $(500, 10)$. Dense fluid reaches closer to the front of the flow as Schmidt number is increased, with the percentage of the flow covered by the $\Delta\tilde{S} = 0.48$ contour increasing from 58% to 88% between the $(Re_I, Sc) = (100, 1)$ and $(Re_I, Sc) = (100, 10)$ cases [further increasing to 100% in the $(100, 100)$ case] and from 80% to 88% between the $(Re_I, Sc) = (500, 1)$ and $(500, 10)$ cases. This demonstrates that increasing Reynolds number reduces the influence of increased Schmidt number on some flow features, with increasing Schmidt number beyond ten having less impact than increasing from 1 to 10. Additionally, this $Sc = 100$ case has dense fluid reaching the very front of the flow. This suggests that a further increase to $Sc = \mathcal{O}(1000)$ to match real-world solute-based flows would likely result in only minor changes in these parameters.

The effect of Reynolds number is more complex (see Fig. 6). While increasing Reynolds number consistently reduces current height (in this case, the decrease at $Sc = 1$ is proportional to $Re^{-0.5}$) and increases the percentage of flow length, the distance between inlet and flow front, covered by the $\Delta\tilde{S} = 0.48$ contour, the percentage of current height covered by the mixed layer increases in the $Re_I = 3000$ case compared with $Re_I = 1000$, perhaps a result of increased mixing by the Kelvin–Helmholtz structures that form with increased Reynolds number (see Fig. 7).

TABLE III. Estimates of the current height (determined by the $\Delta\tilde{S} = 0.03$ contour), the mixed layer thickness as a percentage of current height (defined as the difference in heights of the $\Delta\tilde{S} = 0.03$ and $\Delta\tilde{S} = 0.48$ contours), and the percentage of flow length covered by the $\Delta\tilde{S} = 0.48$ contours. These are based on inspection of Fig. 5. (Brown text indicates the % decrease from the $Sc = 1$ case with the same Re_I, magenta text the % decrease from the $Sc = 10$ case with the same Re_I, and cyan text the % decrease from the $Re_I = 100$ case with the same Sc).

(Re_I, Sc)	$\Delta\tilde{S}^{height}_{0.03}$	$\Delta\tilde{S}^{height}_{0.48}$	$\frac{\Delta\tilde{S}^{height}_{0.03} - \Delta\tilde{S}^{height}_{0.48}}{\Delta\tilde{S}^{height}_{0.03}}$	$\frac{\Delta\tilde{S}^{front}_{0.48}}{\Delta\tilde{S}^{front}_{0.03}}$
(100, 1)	1.20	0.40	67%	58%
(100, 10)	0.77 (36%)	0.48	38%	88%
(100, 100)	0.60 (50%/22%)	0.48	17%	100%
(500, 1)	0.77 (36%)	0.39	50%	80%
(500, 10)	0.60 (22%/22%)	0.40	33%	88%
(1000, 1)	0.67 (44%)	0.39	43%	81%
(3000, 1)	0.63 (48%)	0.21	67%	83%

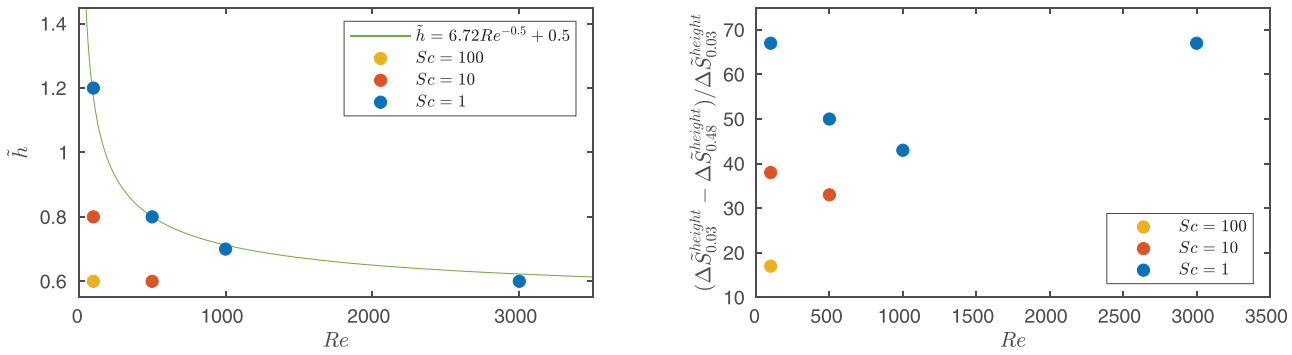

FIG. 6. Scatterplots showing the effect of Reynolds number on (left) current height (where $\tilde{h}$ is the dimensionless current height) and (right) mixed layer size as a percentage of current height, determined by (left) the height of the $\Delta\tilde{S} = 0.03$ contour, and (right) the difference in the heights of the $\Delta\tilde{S} = 0.03$ and $\Delta\tilde{S} = 0.48$ contours at the left-most point of Fig. 5.

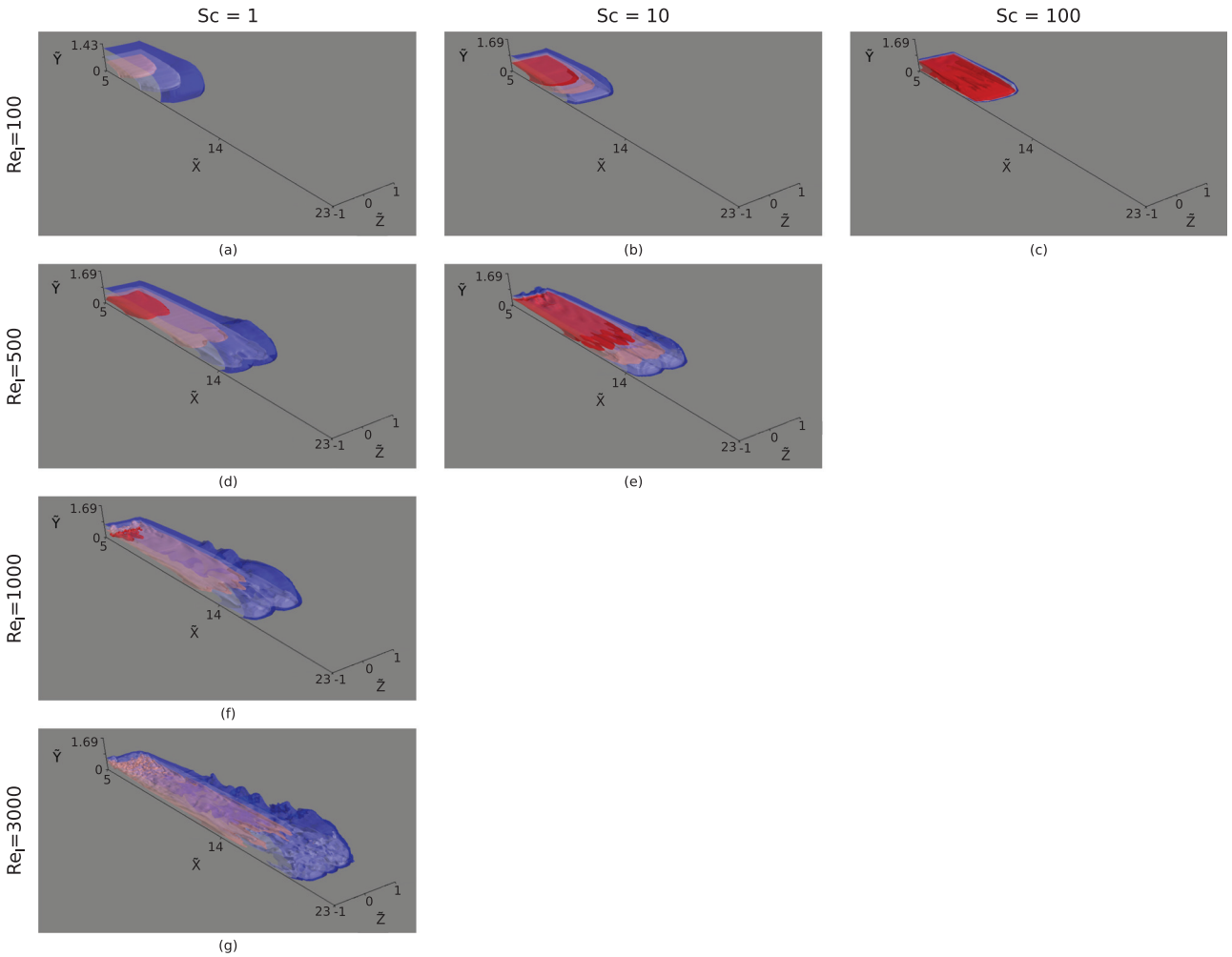

FIG. 7. Three-dimensional isosurfaces of $\Delta\tilde{S}$ at $\tilde{t} = 23.4$ for cases with inlet Reynolds numbers (a)–(c) $Re_I = 100$, (d) and (e) $Re_I = 500$, (f) $Re_I = 1000$, and (g) $Re_I = 3000$, and with Schmidt numbers (a), (d), (f), and (g) $Sc = 1$, (b) and (e) $Sc = 10$, and (c) $Sc = 100$. The isosurfaces shown are (blue to red) $\Delta\tilde{S} = 0.02$, $\Delta\tilde{S} = 0.25$, $\Delta\tilde{S} = 0.48$, and $\Delta\tilde{S} = 0.71$.

These structures are also present in the $Re_I = 1000$ case and may be emerging in the $(Re_I, Sc) = (500, 10)$ case, in which the mixed layer thickness decreases as a proportion of current height compared with the lower Re_I cases. However, the rate of decrease between $Re_I = 500$ and $Re_I = 1000$ is slower than that between $Re_I = 100$ and $Re_I = 500$, which may also be a result of the Kelvin–Helmholtz structures.

The three-dimensional density isosurfaces (Fig. 7) indicate that these trends extend across the width of the tank. These isosurfaces show signs of structural change with increasing Reynolds and Schmidt numbers. At $Re_I = 100$, the isosurfaces from the cases with $Sc = 1$ and $Sc = 10$ are completely smooth. At $Sc = 100$, ridges appear in the highest density isosurface. In the $(Re_I, Sc) = (1000, 1)$ case, the lowest density isosurface has oscillations behind the head. By $(Re_I, Sc) = (3000, 1)$, all isosurfaces have lost the smoothness of the $(Re_I, Sc) = (100, 1)$ case, as expected owing to the increase in turbulence. Therefore, depending on the flow Reynolds and Schmidt numbers, perturbations may be visible in the highest and/or lowest density isosurfaces. Additionally, with increasing Reynolds number the perturbations in the density isosurfaces are most pronounced near the head, while for increasing Schmidt number the perturbations become more pronounced with increasing distance from the head. This suggests that there are at least two distinct mechanisms influencing the flow structure.

To investigate the mechanisms responsible for these changes, pseudocolor plots of density both in an $\tilde{X} - \tilde{Z}$ plane at $\tilde{Y} = 0.1$ and in a $\tilde{Z} - \tilde{Y}$ plane near the current front (Fig. 8) can be inspected. These plots show that cases $(Re_I, Sc) = (100, 100), (500, 10)$, and $(3000, 1)$ contain regions of less-dense fluid surrounded by the denser fluid of the head. The $\tilde{Z} - \tilde{Y}$ plane illustrates that this fluid is absorbed upward, originating from the over-running of ambient by the raised nose of the flow. Therefore, as well as causing dense fluid to reach closer to the front of the flow, increasing Schmidt number at fixed Reynolds number leads to the formation of lobe-and-cleft structures within the head. These structures also form with increasing Reynolds number.

B. Velocity

In order to obtain a thorough understanding of the flow structure, the velocity structures are inspected. Pseudocolor plots of all three velocity components for each case are shown on an $\tilde{X} - \tilde{Z}$ slice close to the bottom boundary (Fig. 9) and on $\tilde{X} - \tilde{Y}$ slices (Figs. 10 and 11). In addition to Figs. 7 and 8, Fig. 9 highlights a strong symmetry about the central $\tilde{Z}$-plane in all but the $(Re_I, Sc) = (3000, 1)$ case. Only in this case does the increase in nonlinearity owing to higher Reynolds number cause this symmetry to break. Excepting this highest Reynolds number case, the cross-stream velocity for all cases has negligible magnitude on the central $\tilde{Z} = 0$ plane (Fig. 10), indicating a symmetric solution. However, away from this central plane, the magnitude of cross-stream and vertical velocities have equivalent magnitude in all cases (for example the plane at $\tilde{Z} = 0.5$ shown in Fig. 11). This suggests that the flow is not two-dimensional as commonly assumed.[1,8] Downstream velocity on the two $\tilde{X} - \tilde{Y}$ planes has the same structure and magnitude in all cases, as does cross-stream velocity in the $Re_I = 3000$ case.

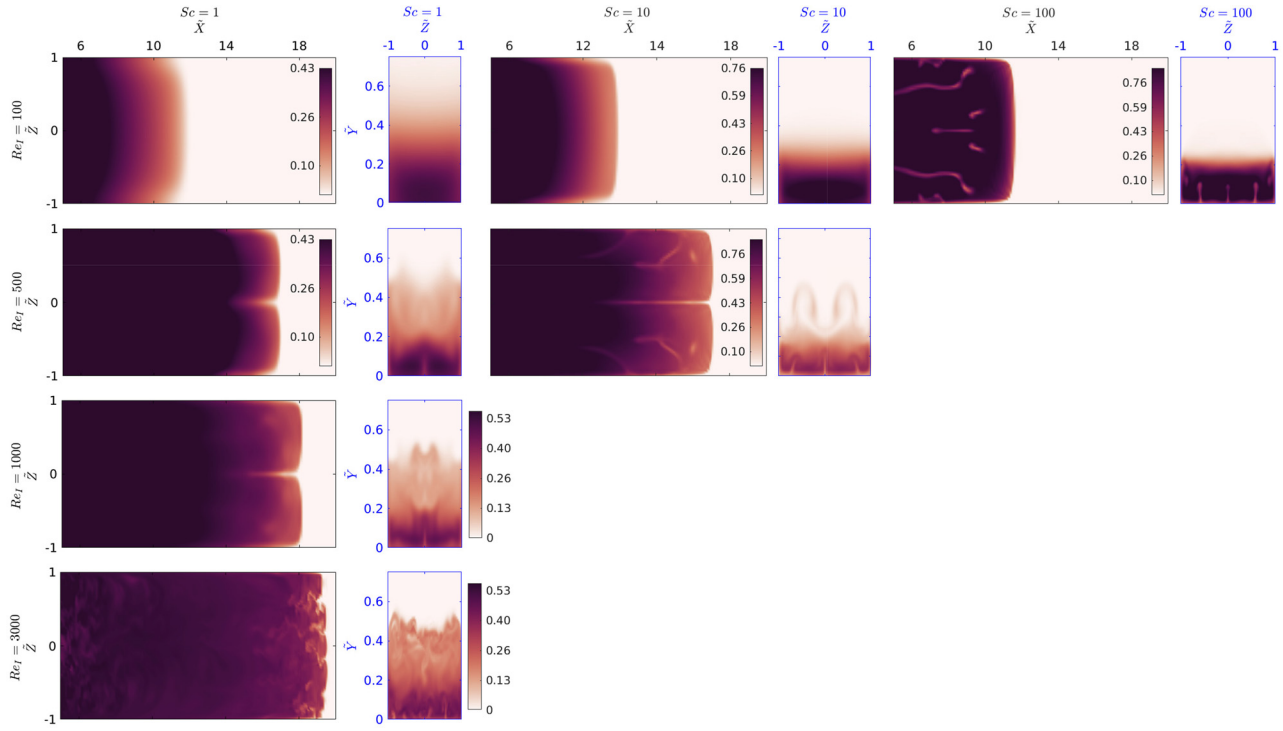

FIG. 8. Pseudocolor plots of $\Delta\tilde{S}$ at $\tilde{t} = 23.4$ on an $\tilde{X} - \tilde{Z}$ plane at $\tilde{Y} = 0.1$ and a $\tilde{Z} - \tilde{Y}$ plane $\tilde{X} = 2$ behind the current front for (top to bottom) increasing Reynolds number and (left to right) increasing Schmidt number.

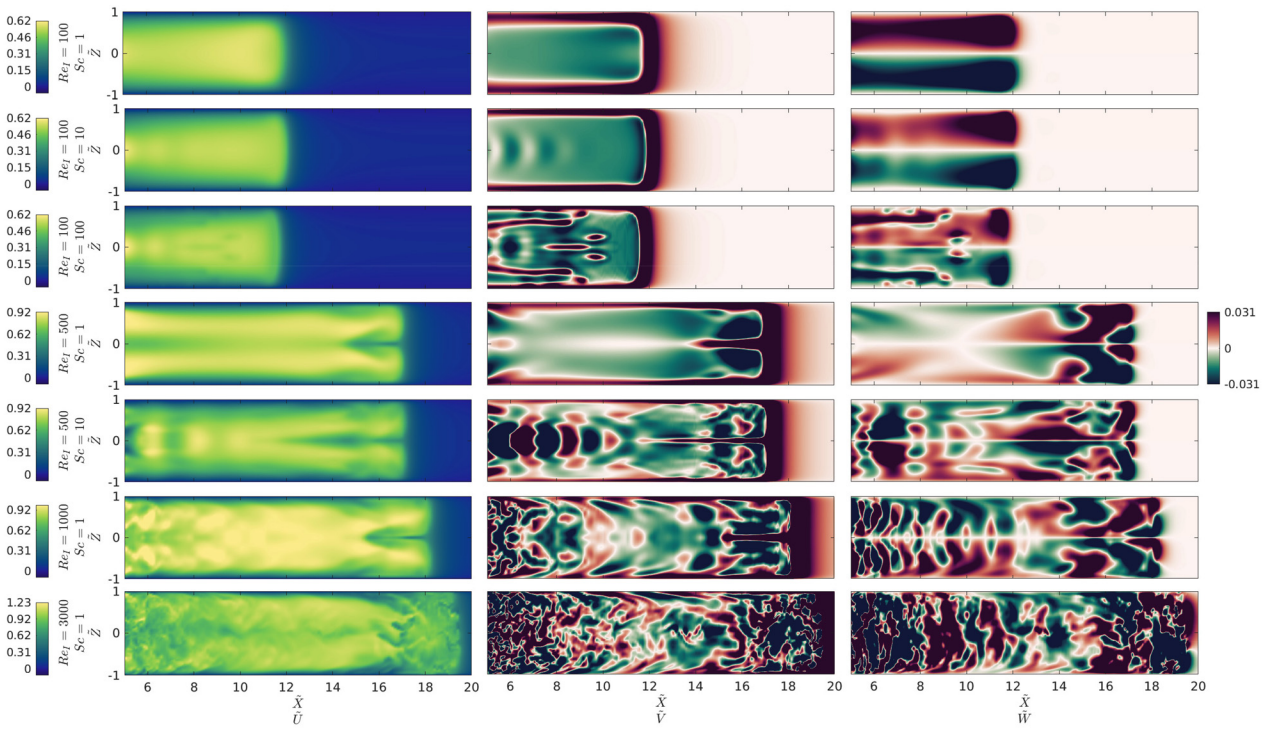

FIG. 9. Plots of (left) downstream, (center) vertical, and (right) cross-stream velocity for each case at $\tilde{t} = 23.4$ on an $\tilde{X} - \tilde{Z}$ slice at $\tilde{Y} = 0.1$.

The vertical velocity plots confirm the over-riding of ambient fluid, with Fig. 9 showing areas of large positive vertical velocity close to the bottom boundary and near the front of the current for the $(Re_I, Sc) = (100, 100)$, (500, 10), and (3000, 1) cases, corresponding to the rising buoyant fluid over-ridden by the current front. Additionally, as expected from the density contours, increasing Reynolds number increases downstream velocity within the flow. Increasing Reynolds number also increases variation in all components of velocity within the body, including alternating positive and negative vertical velocity near the side walls in the $Re_I = 1000, 3000$ cases. Visible in both Figs. 9 and 10, increasing Schmidt number results in a regular alternating pattern of positive and negative vertical velocity at a central cross-stream location, and corresponding positive and negative cross-stream velocity on either side of the center, behind the head of the current. The regular alternating vertical velocity pattern established by increasing Schmidt number is localized to the cross-stream center of the flow, though increasing Reynolds number increases the width of the motions (Figs. 9 and 11).

Figure 12 illustrates the flow behind the head in the $(Re_I, Sc) = (500, 1)$, $(500, 10)$ cases at $\tilde{t} = 66.3$, demonstrating that these are not short-term changes. As well as velocity plots, this figure contains plots of density fluctuations from cross-stream averaged density $(\Delta\tilde{S} - \overline{\Delta\tilde{S}}_{\tilde{Z}}$, where $\overline{\Delta\tilde{S}}_{\tilde{Z}}$ is density averaged in the cross-stream direction). The density fluctuations in the $Sc = 10$ case contain a pattern of alternating positive and negative regions correlated with those in vertical velocity but with a 1/4-wavelength offset (characteristic of internal gravity waves[61]). To understand why decreasing mass diffusivity leads to large-scale changes in flow structure, plots of swirling strength and gradient Richardson number will be inspected.

Figure 13 shows plots of swirling strength ζ_{ci} as defined by Zhou *et al.*,[62]

$$L = \begin{bmatrix} \frac{\partial U}{\partial X} & \frac{\partial U}{\partial Y} & \frac{\partial U}{\partial Z} \\ \frac{\partial V}{\partial X} & \frac{\partial V}{\partial Y} & \frac{\partial V}{\partial Z} \\ \frac{\partial W}{\partial X} & \frac{\partial W}{\partial Y} & \frac{\partial W}{\partial Z} \end{bmatrix} = [\chi_r \chi_{cr} \chi_{ci}] \begin{bmatrix} \zeta_r & 0 & 0 \\ 0 & \zeta_{cr} & \zeta_{ci} \\ 0 & -\zeta_{ci} & \zeta_{cr} \end{bmatrix} [\chi_r \chi_{cr} \chi_{ci}]^T, \tag{5}$$

where L is the velocity gradient tensor, ζ_r and χ_r are the real eigenvalue and eigenvector, and $\zeta_{cr} \pm i\zeta_{ci}$ the complex conjugate pair of complex eigenvalues with corresponding eigenvectors $\chi_{cr} \pm i\chi_{ci}$. These plots reveal that increasing Schmidt number leads to the formation of structures in the mixed layer between the current and the ambient in the center of the tank in the cross-stream direction (with the mixed layer here defined as the region between the $\Delta\tilde{S} = 0.03$ and $\Delta\tilde{S} = 0.48$ contours). The placement of these structures is identical for the $(Re_I, Sc) = (100, 10), (100, 100)$ cases, and their spacing in the downstream direction is the same for all three $Sc > 1$ cases. Figure 13 shows that increasing Reynolds number also leads to the formation of structures within the body, though they differ from those resulting from increased Schmidt number. While some of the structures resulting from increased Reynolds number are within the mixed region, the structures in the higher Reynolds number cases have a less regular

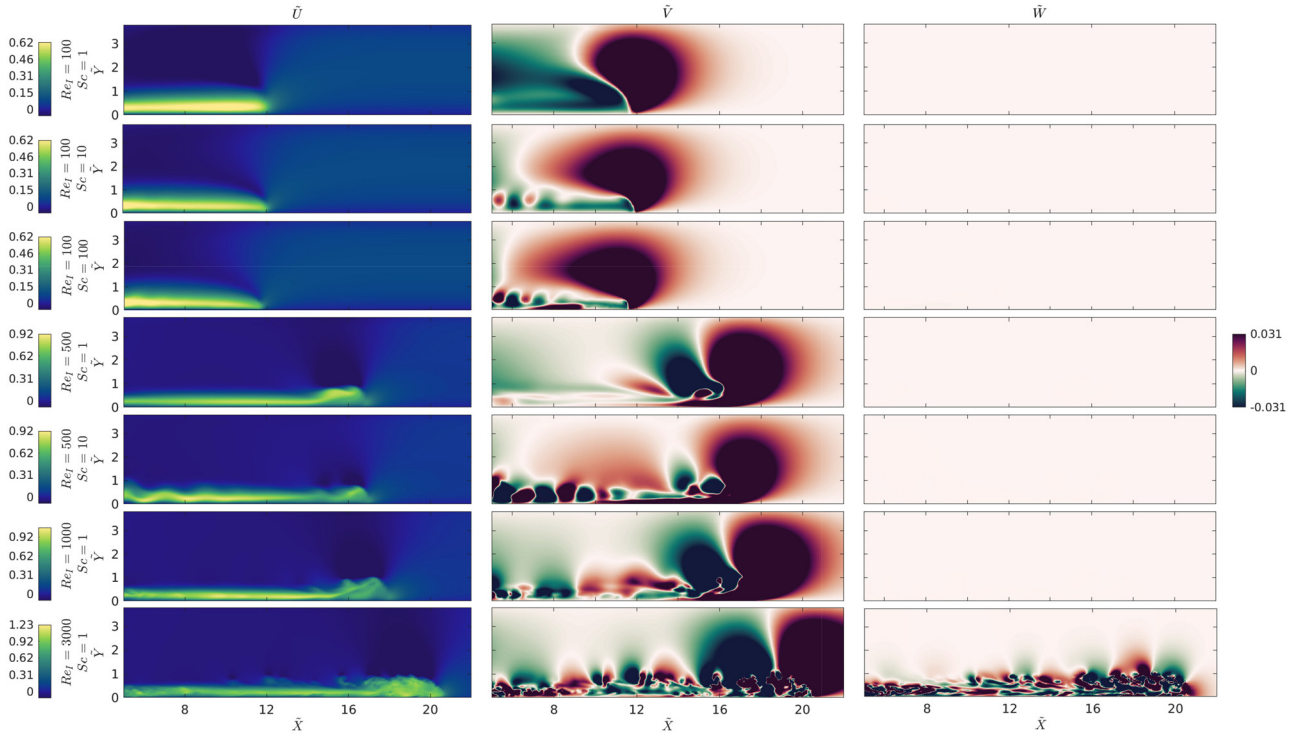

FIG. 10. Plots of (left) downstream, (center) vertical, and (right) cross-stream velocity for each case at $\tilde{t} = 23.4$ on an $\tilde{X} - \tilde{Y}$ slice at a central cross-stream location ($\tilde{Z} = 0$).

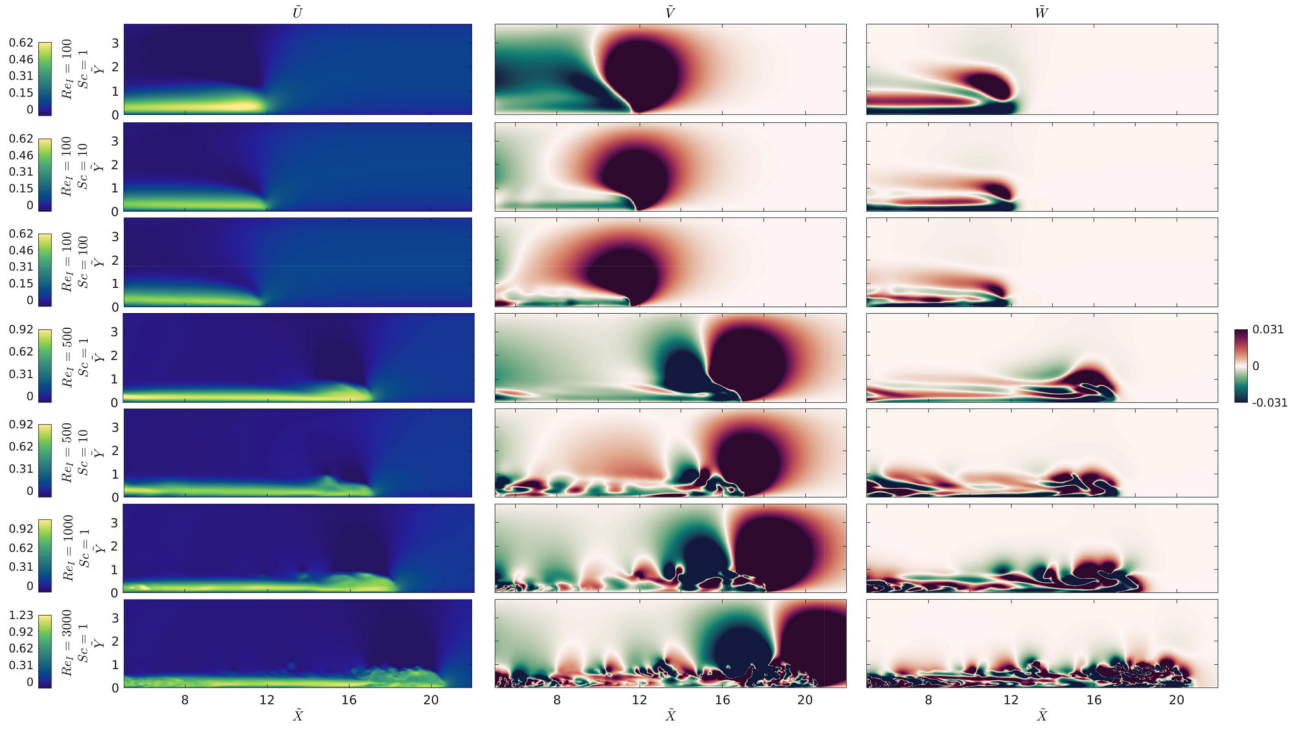

FIG. 11. Plots of (left) downstream, (center) vertical, and (right) cross-stream velocity for each case at $\tilde{t} = 23.4$ on an $\tilde{X} - \tilde{Y}$ slice at an off-center cross-stream location ($\tilde{Z} = 0.5$).

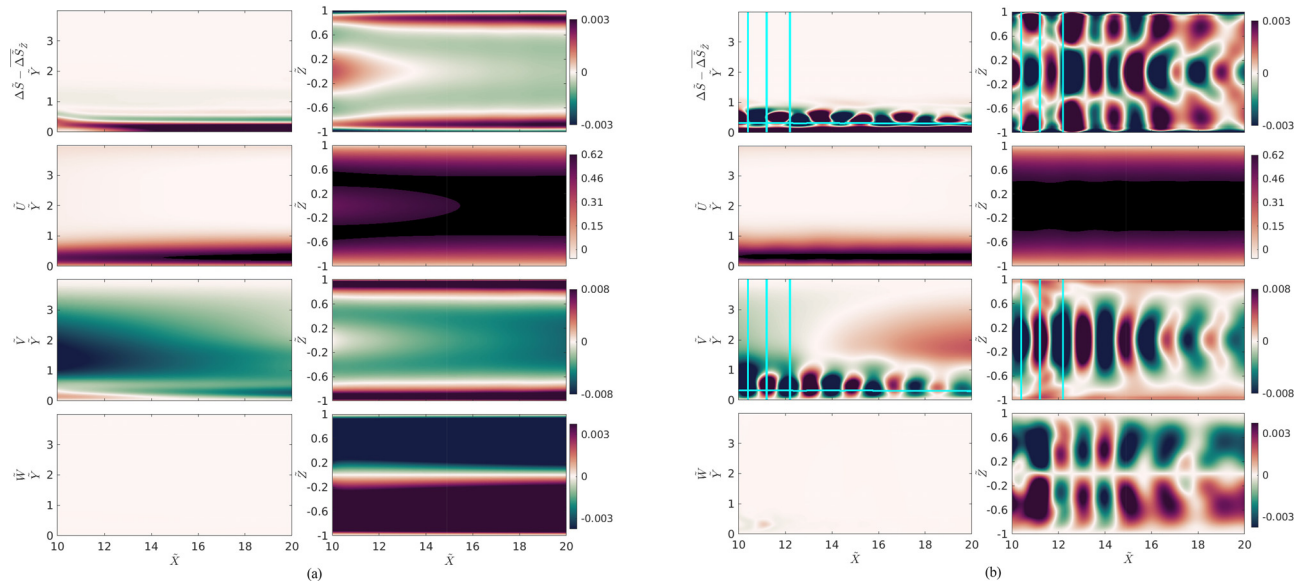

FIG. 12. Comparison of the cases with (a) $(Re_I, Sc) = (500, 1)$ and (b) $(Re_I, Sc) = (500, 10)$ at $\tilde{t} = 66.3$ on (left) a central cross-stream plane and (right) a plane perpendicular to the lower boundary at $\tilde{Y} = 0.35$. From top to bottom, the plots are excess density fluctuations from the cross-stream average value (where the cross-stream average density is denoted by $\overline{\Delta\tilde{S}}_{\tilde{Z}}$), and downstream, vertical, and cross-stream velocities. The horizontal lines indicate the height of the downstream velocity maximum, and vertical lines show the approximate downstream locations of $\Delta\tilde{S} - \overline{\Delta\tilde{S}}_{\tilde{Z}} = 0$.

pattern (with a different physical spacing to the high Schmidt number cases) and are not limited to the center in the cross-stream direction.

Change in large-scale flow structures with Schmidt number is not immediately anticipated, given that Schmidt number is expected to result in changes at the small scale. Figure 14 shows the density and downstream velocity profiles on a central cross-stream location averaged over downstream location at the time step illustrated in Fig. 12. The change in diffusivity resulting from the Schmidt number increase leads to a change in density profile, specifically the anticipated increase in density in the lower part of the flow and sharper transition from dense to ambient fluid. As there is a greater density difference, there is a corresponding increase in downstream velocity within the body. These changes may affect the stability of the interface. To illustrate this, a gradient Richardson number can be calculated,

$$Ri = \frac{g}{\rho_c} \frac{\partial \bar{\rho}/\partial Y}{(\partial \bar{U}/\partial Y)^2}, \tag{6}$$

where ρ_c is the density of the fluid pumped in at the inlet, which gives a measure of the stability of density stratification. If $Ri > 0.25$, then the energy produced by shear is not sufficient to overcome the density stratification and is therefore dissipated.[63] Profiles of Ri for the cases with $Re_I = 500$ are shown in Fig. 14(c). Increasing Schmidt number from 1 changes the Ri profile such that the value at the current height moves from above to below this critical level. The same change is seen for every case with $Sc > 1$, while for every case with $Sc = 1$, $Ri > 0.25$ in this area. Therefore, changes in the density and velocity profiles resulting from decreasing mass diffusivity (and therefore increasing Schmidt number) lead to the density stratification becoming less stable such that energy produced from shear is no longer dissipated but instead leads to large-scale structural changes in the flow.

IV. DISCUSSION

Increasing the flow Reynolds number has been shown to result in a shorter head, with more velocity fluctuations, and greater front and internal velocities. Excepting the highest Reynolds number case considered in this work, a strong symmetry plane is present at a central cross-stream location for all cases. Attempting to quantify such flows using exclusively a central cross-stream plane could, depending on flow Reynolds number, give a misleading impression of the overall flow particularly in terms of the cross-stream velocity (Figs. 9–11). For most cases, W was found to be 0 on the central cross-stream plane but elsewhere the magnitude of cross-stream velocity was equivalent to that of vertical velocity suggesting that the flow is not two-dimensional as often assumed.[1,8]

A. The effect of Reynolds and Schmidt numbers on flow in the head

Figure 5 and Table III show that increasing either Schmidt or Reynolds number results in a more defined head, with a forward angled depression in the density contour behind the head. The head height, based on the $\Delta\tilde{S} = 0.03$ density contour, decreases slightly from $\tilde{Y} \approx 1.2$ at $Re_I = 100$ to $\tilde{Y} = 1$ at $Re_I = 500$ with no further decrease when Reynolds number is increased further. Increasing Schmidt number does consistently reduce the head height, with a more significant change at lower Reynolds number and when Schmidt number is increased from 1 to 10 compared with 10 to 100. The difference between the rightmost positions of the $\Delta\tilde{S} = 0.03$ and

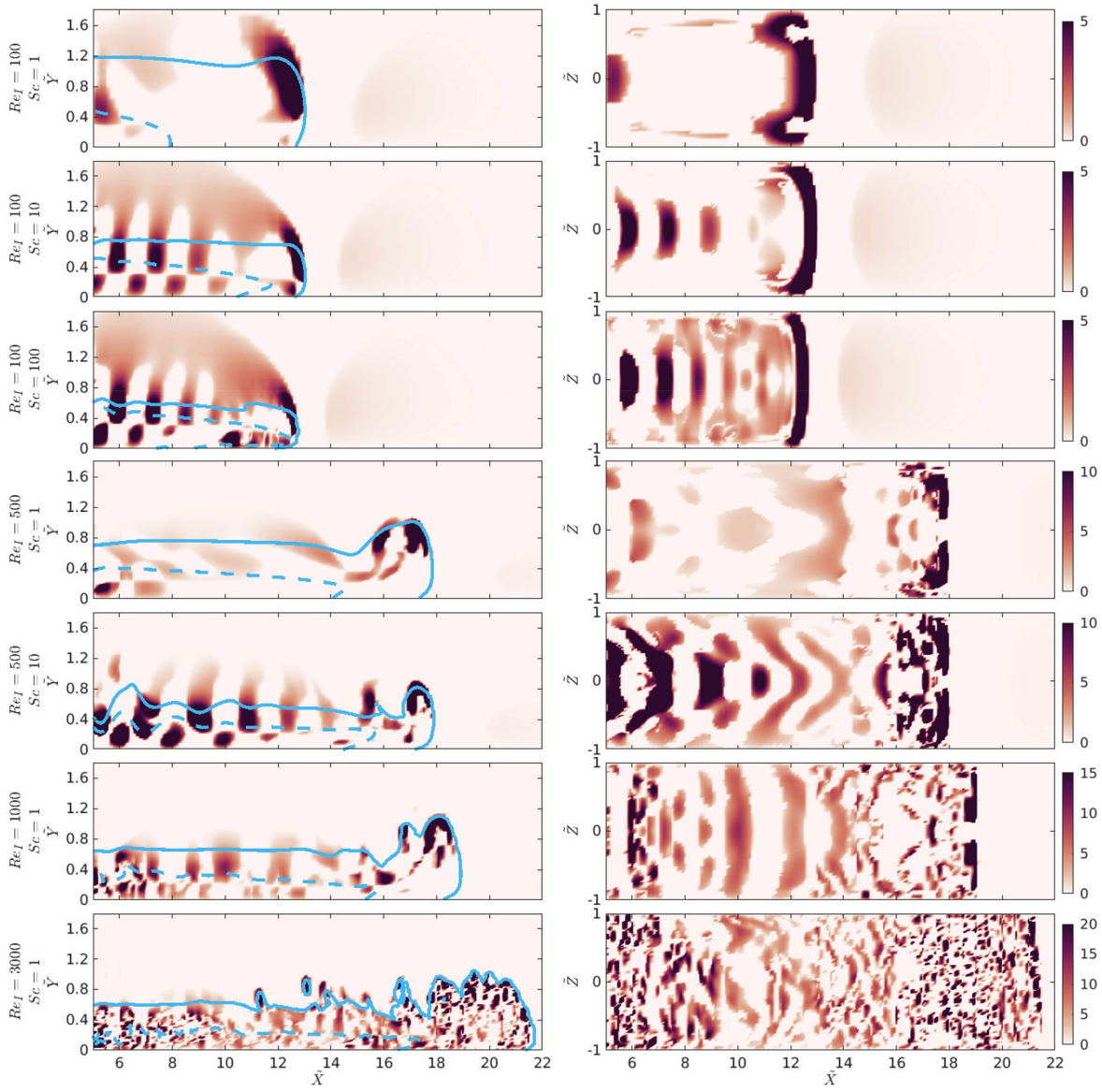

FIG. 13. Pseudocolor plots of swirling strength at $\tilde{t} = 23.4$ for each case (left) on an $\tilde{X} - \tilde{Y}$ plane at a central cross-stream location, and (right) on an $\tilde{X} - \tilde{Z}$ plane at $\tilde{Y} = 0.5$. The blue lines illustrate the (solid) $\Delta\tilde{S} = 0.03$ and (dashed) $\Delta\tilde{S} = 0.48$ excess density contours.

$\Delta\tilde{S} = 0.48$ contours as a proportion of current front position decreases with both increased Reynolds and Schmidt numbers, indicating that dense fluid is reaching closer to the front of the flow. In the $(Re_I, Sc) = (100, 100)$ case, the $\Delta\tilde{S} = 0.48$ contour reaches the front of the flow, suggesting that a further increase in Schmidt number would likely have little impact.

The lobe-and-cleft structures resulting from the over-running of ambient fluid by the current front are present in some cases but not others (Fig. 8). As lobe-and-cleft structures are associated with some of the largest bed shear stresses,[22,64] and changes in rates of mixing,[65] accurately capturing this feature is important to understanding the flow structure. While the $(Re_I, Sc) = (100, 1)$, $(100, 10)$, and $(500, 1)$ cases do not exhibit over-running of ambient fluid, the $(Re_I, Sc) = (100, 100)$ and $(500, 10)$ cases do. Therefore, for Reynolds numbers $\mathcal{O}(100)$ the presence of lobes-and-clefts in the current head is dependent on the Schmidt number [with Fig. 15(b) showing the phase space where these structures are found in this work]. This conflicts with the findings of Bonometti and Balachandar,[33] who suggest that lobe-and-cleft structures are not Schmidt number dependent. However, varying Schmidt number in three-dimensional DNS here was only possible at Reynolds numbers sufficiently low that these structures were not already present at $Sc = 1$. As over-running of ambient fluid is observed

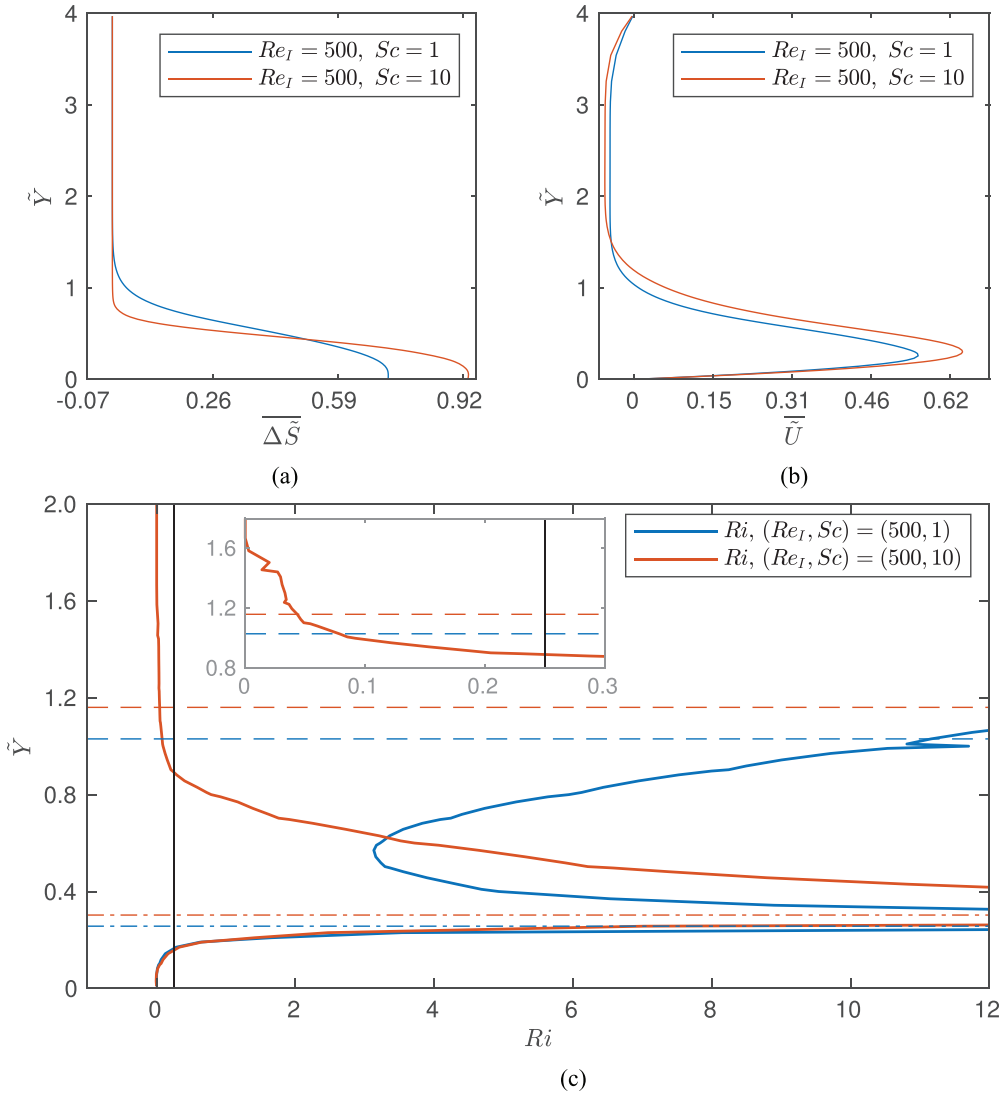

FIG. 14. Comparison of (a) excess density and (b) downstream velocity averaged over downstream locations at the time step illustrated in Fig. 12, and (c) *Ri* profile for the cases with $(Re_I, Sc) = (500, 1)$ and (500, 10) based on the excess density and velocity profiles shown in (a) and (b). The horizontal lines show (dashed) the height of the current based on where the average downstream velocity profile changes from positive to negative, and (dot-dash) the average height of the maximum downstream velocity, and the vertical line indicates the critical value of $Ri = 0.25$. The inset shows a magnified view of the high Schmidt number case plot near the upper interface, illustrating where flow *Ri* moves from above to below the critical value.

in the $(Re_I, Sc) = (3000, 1)$ case (Fig. 8), providing the Reynolds number of the flow is sufficiently high this flow feature may be captured without increasing Schmidt number above 1.

B. The effect of Reynolds and Schmidt numbers on flow behind the head

Considering flow behind the head, the current height decreases with both Reynolds and Schmidt numbers (Fig. 5 and Table III). However, the height of the $\Delta\tilde{S} = 0.48$ contour seems to be relatively consistent regardless of the Reynolds and Schmidt number of the flow (likely a result of the short duration of the simulations presented). Increasing Reynolds number from $Re_I = 100$ to $Re_I = 500$ leads to a smaller percentage decrease in current height as Schmidt number is increased. At the Reynolds and Schmidt number range considered in this work, the percentage change in thickness of the mixed layer of fluid behind the head as Schmidt number is increased from 1 to 10 is equivalent in both $Re_I = 100$ and $Re_I = 500$ cases. A further increase from $Sc = 10$ to $Sc = 100$, however, results in a smaller change. Increasing Reynolds number was found to have a more complex effect on mixed layer thickness, with the percentage of flow height taken up by the mixed layer initially decreasing and then increasing when $Re_I = 3000$. This may be a result of increased mixing from the

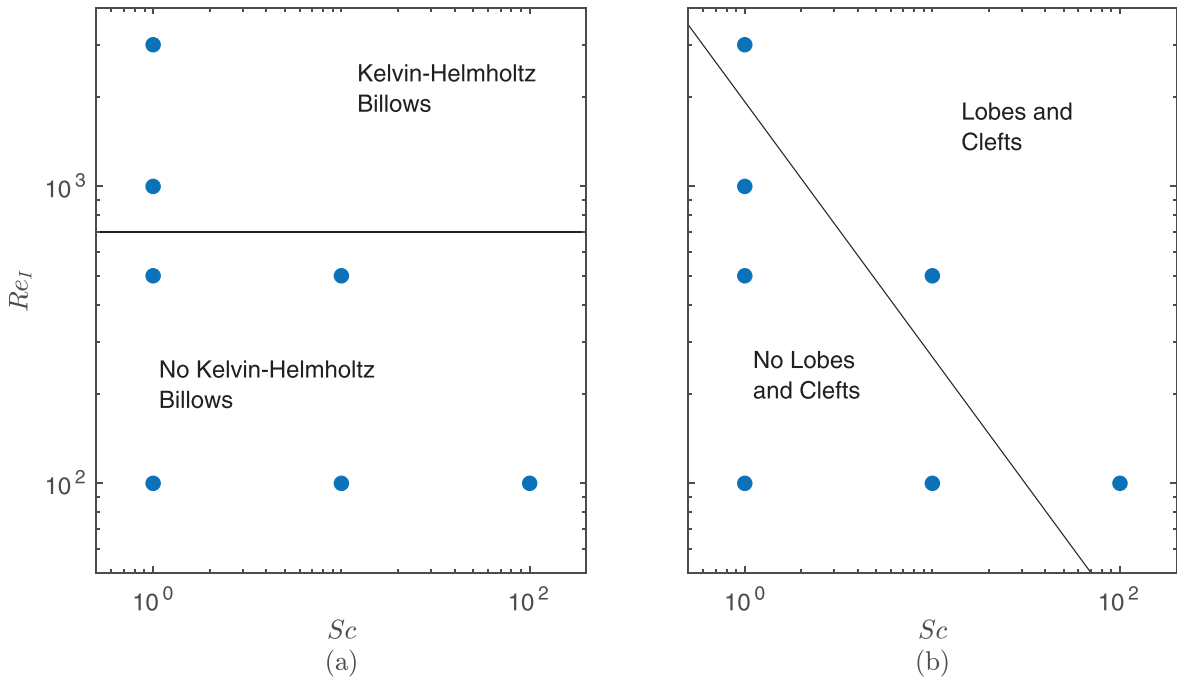

FIG. 15. Scatterplots showing the Schmidt and Reynolds numbers where (a) Kelvin–Helmholtz structures, and (b) lobe-and-cleft structures are present in Fig. 7.

Kelvin–Helmholtz structures (visible in Fig. 7) that begin to form as Re_I increases. Close examination of the density contours in Fig. 5 and the isosurfaces in Fig. 7 indicates that the Kelvin–Helmholtz structures may be emerging in the $(Re_I, Sc) = (500, 10)$ case [but not the $(Re_I, Sc) = (500, 1)$ case]. This suggests that increasing Schmidt number may reduce flow stability.

Several changes resulting from increased Schmidt number have been noted in the data from this paper. In many cases, the impact of increasing Schmidt number beyond one is either reduced by increasing Reynolds number (for example the change in current height), or the same changes are observed with increased Reynolds number (for example the presence of lobes-and-clefts). There are, however, features that are not captured if $Sc = 1$ is assumed. In particular, increasing Schmidt number is related to the formation of structures at the current–ambient interface behind the head. This can be seen in several of the plots presented, for example, the instability of the density contours (Fig. 5), in the velocity plots (Figs. 9 and 10), and in the swirling strength plots (Fig. 13), in which wave-like distortions in the density contours correlate with peaks in swirling strength.

The stability of the interface can be quantified by a gradient Richardson number in the upper part of the flow. In all cases with $Sc = 1$, even those with Kelvin–Helmholtz structures behind the head, the gradient Richardson number in the upper part of the flow is above the critical value. As discussed by Pelmard *et al.*,[24] a gradient Richardson number below 0.25 in the head may lead to the formation of Kelvin–Helmholtz structures that then dissipate some distance behind the head if the value rises above the critical level in the body. Therefore, the current–ambient interface in the body may be stable even with the presence of Kelvin–Helmholtz structures near the head. All cases with $Sc > 1$ have $Ri < 0.25$ in the upper part of the flow, suggesting that density stratification is no longer stable enough to dissipate the energy generated through shear and exhibit the formation of corresponding structures on the current–ambient interface behind the head. These structures are not diminished as distance from the head increases (Fig. 13), suggesting that this may be a distinct mechanism from the formation of Kelvin–Helmholtz vortices, the influence of which decreases with distance from the head in these data, and which are present in some cases with $Sc = 1$ [see Fig. 15(a)]. A similar change from above to below the critical gradient Richardson number (with corresponding structure formation) was observed by Kneller *et al.*[66] in particulate flows, both with increasing bed slope and increasing particle settling velocity (or larger particle sizes).

The velocity and density perturbations associated with the structures in the cases with $Ri < 0.25$ (Fig. 12) have correlated patterns of alternating positive and negative regions, with the $1/4-$ wavelength offset characteristic of internal gravity waves,[61] supporting the conclusions of Marshall *et al.*[25] The formation of these internal gravity waves is a result of the decrease in mass diffusivity sharpening the density profile, leading to a change in the stability of the interface. Crucially, unlike other characteristics, it does not appear to be the case that this effect of increased Schmidt number is diminished by increased Reynolds number in the range considered here. The perturbations in density field are at least as prominent in the $Re_I = 500$ case as in the $Re_I = 100$ cases (Fig. 5). The effect is also not captured purely by increasing Reynolds number in the range considered in this work. While peaks in swirling strength are found in the $Re_I = 1000$, 3000 cases, they are missing the regularity of those in the higher Sc cases and are not limited to the center in the cross-stream direction, supporting the suggestion that this is a separate mechanism to those seen with increased Reynolds number.

V. CONCLUSIONS

Many numerical investigations of gravity current flows have sought to mitigate the high computational cost of three-dimensional direct numerical simulation by claiming the effect of increasing Schmidt number from 1 is negligible. However, the justifiability of this assumption has been questionable given the lack of understanding regarding the effect of Schmidt number on three-dimensional flow features. In this work, the effects of Reynolds and Schmidt numbers on constant-influx solute-based gravity current flow structure have been investigated through three-dimensional direct numerical simulation performed using the spectral element solver Nek5000. These results have been used to draw conclusions regarding when a $Sc = 1$ assumption is justified.

The importance of considering Schmidt number is dependent on the flow property of interest and on the flow itself. Some flow features appear to be independent of Schmidt number (for example, current front velocity). Additionally, some of the effects of increased Schmidt number also occur with increased Reynolds number (such as the appearance of lobe-and-cleft structures in the head) or are reduced by increased Reynolds number (such as the change in current height). A notable exception is the reduction in gradient Richardson number. In flows with $Re_I = 100$ and 500, increasing Schmidt number from 1 to 10 was found to reduce the gradient Richardson number in the body of the flow from above to below the critical value, resulting in the presence of structures in the mixed layer. When moving from $Re_I = 100$ to $Re_I = 500$, this effect of increased Schmidt number was not reduced. Further, equivalent structures were not apparent in the $Re_I = 3000$ case, suggesting that this feature may not be captured purely by increasing Reynolds number. When considering the structure of the gravity current body in a high Schmidt number flow, assuming $Sc = 1$ may therefore lead to qualitative changes in flow structure (for example, to internal gravity waves). The importance of considering Schmidt number may also depend on flow type, for example, the data presented in this work suggest that Schmidt number impact may be greater in a more viscous flow (such as clay based transitional flows[67,68]) though further work considering the impact of Reynolds number on such flows is needed.

A Schmidt number of 1 is often assumed when performing numerical investigations of gravity current flows. This is largely as a result of the rapidly escalating computational cost of DNS,[27,34] which scales with Re^3Sc^2. When computational resources are limited, deciding whether to prioritize increasing Schmidt or Reynolds number is a complex issue dependent on several factors. There may be no benefit to prioritizing Schmidt number at the expense of Reynolds number if data analysis will focus on parameters that are not Schmidt number dependent (such as front velocity), or that are also seen with increased Reynolds number (such as the formation of lobe-and-cleft structures). However, it is recommended to have Schmidt number sufficiently large to accurately capture the body gradient Richardson number. The work presented here suggests that assuming a Schmidt number of 1 in numerical investigations leads to substantial structural differences compared with higher Schmidt number flows. However, even at $Re_I = 100$ the effect of increasing Schmidt number from 10 to 100 was quantitative rather than qualitative [similar to the findings of Deepwell and Stastna[47] for flow along a pycnocline(s)], and therefore the structure of solute-based flows [$Sc = \mathcal{O}(1000)$] can likely be captured with the comparatively minor cost of a small increase in Schmidt number rather than the large cost of matching Schmidt number exactly.

ACKNOWLEDGMENTS

We thank the reviewers and editor for their feedback on this paper. The numerical simulations presented were carried out on the ARC3 and ARC4 supercomputing facilities at the University of Leeds. This work was supported by the Engineering and Physical Sciences Research Council (EPSRC) Centre for Doctoral Training in Fluid Dynamics at the University of Leeds, Grant No. EP/L01615X/1. R.M.D. was supported by the NERC Grant No. NE/S014535/1. S.D. would like to acknowledge the computer time provided by NCSA, UIUC on the Blue Waters supercomputer at NCSA, which was used for the initial setup and testing of the numerical simulations.

The authors have no conflicts to disclose.

DATA AVAILABILITY

The data that support the findings of this study are available from the corresponding author upon reasonable request.

REFERENCES

[1]J. E. Simpson, *Gravity Currents: In the Environment and the Laboratory* (Cambridge University Press, 1997).
[2]M. Ungarish, *An Introduction to Gravity Currents and Intrusions* (Chapman and Hall/CRC, 2009).
[3]R. E. Britter and P. F. Linden, "The motion of the front of a gravity current travelling down an incline," J. Fluid Mech. **99**, 531–543 (1980).
[4]R. M. Dorrell, J. Peakall, S. E. Darby, D. R. Parsons, J. Johnson, E. J. Sumner, R. B. Wynn, E. Özsoy, and D. Tezcan, "Self-sharpening induces jet-like structure in seafloor gravity currents," Nat. Commun. **10**, 1381 (2019).
[5]P. J. Talling, "On the triggers, resulting flow types and frequencies of subaqueous sediment density flows in different settings," Mar. Geol. **352**, 155–182 (2014).
[6]M. I. Cantero, J. R. Lee, S. Balachandar, and M. H. García, "On the front velocity of gravity currents," J. Fluid Mech. **586**, 1–39 (2007).
[7]A. J. Hogg, M. M. Nasr-Azadani, M. Ungarish, and E. Meiburg, "Sustained gravity currents in a channel," J. Fluid Mech. **798**, 853–888 (2016).
[8]E. Meiburg, S. Radhakrishnan, and M. Nasr-Azadani, "Modeling gravity and turbidity currents: Computational approaches and challenges," Appl. Mech. Rev. **67**, 040802 (2015).
[9]T. M. Özgökmen, P. F. Fischer, J. Duan, and T. Iliescu, "Three-dimensional turbulent bottom density currents from a high-order nonhydrostatic spectral element model," J. Phys. Oceanogr. **34**, 2006–2026 (2004).
[10]M. W. Stacey and A. J. Bowen, "The vertical structure of density and turbidity currents: Theory and observations," J. Geophys. Res. **93**, 3528–3542, https://doi.org/10.1029/JC093iC04p03528 (1988).
[11]Z. He, L. Zhao, R. Zhu, and P. Hu, "Separation of particle-laden gravity currents down a slope in linearly stratified environments," Phys. Fluids **31**, 106602 (2019).
[12]A. Dai and C.-S. Wu, "High-resolution simulations of unstable cylindrical gravity currents undergoing wandering and splitting motions in a rotating system," Phys. Fluids **30**, 026601 (2018).
[13]R. Ouillon, E. Meiburg, and B. R. Sutherland, "Turbidity currents propagating down a slope into a stratified saline ambient fluid," Environ. Fluid Mech. **19**, 1143–1166 (2019).
[14]B. Kneller and C. Buckee, "The structure and fluid mechanics of turbidity currents: A review of some recent studies and their geological implications," Sedimentology **47**, 62–94 (2000).
[15]M. Azpiroz-Zabala, M. J. B. Cartigny, P. J. Talling, D. R. Parsons, E. J. Sumner, M. A. Clare, S. M. Simmons, C. Cooper, and E. L. Pope, "Newly recognized turbidity current structure can explain prolonged flushing of submarine canyons," Sci. Adv. **3**, e1700200 (2017).
[16]E. J. Sumner, J. Peakall, R. M. Dorrell, D. R. Parsons, S. E. Darby, R. B. Wynn, S. D. McPhail, J. Perrett, A. Webb, and D. White, "Driven around the bend: Spatial evolution and controls on the orientation of helical bend flow in a natural submarine gravity current," J. Geophys. Res. **119**, 898–913, https://doi.org/10.1002/2013JC009008 (2014).

[17]E. Özsoy, D. D. Iorio, M. C. Gregg, and J. O. Backhaus, "Mixing in the Bosphorus Strait and the Black Sea continental shelf: Observations and a model of the dense water outflow," J. Mar. Syst. **31**, 99–135 (2001).
[18]V. K. Birman and E. Meiburg, "High-resolution simulations of gravity currents," J. Braz. Soc. Mech. Sci. Eng. **28**, 169–173 (2006).
[19]C. Härtel, E. Meiburg, and F. Necker, "Analysis and direct numerical simulation of the flow at a gravity-current head. Part 1. Flow topology and front speed for slip and no-slip boundaries," J. Fluid Mech. **418**, 189–212 (2000).
[20]M. I. Cantero, S. Balachandar, M. H. García, and D. Bock, "Turbulent structures in planar gravity currents and their influence on the flow dynamics," J. Geophys. Res. **113**, C08018, https://doi.org/10.1029/2007JC004645 (2008).
[21]K. Bhaganagar, "Role of head of turbulent 3-D density currents in mixing during slumping regime," Phys. Fluids **29**, 020703 (2017).
[22]F. Necker, C. Härtel, L. Kleiser, and E. Meiburg, "High-resolution simulations of particle-driven gravity currents," Int. J. Multiphase Flow **28**, 279–300 (2002).
[23]T. M. Özgökmen, P. F. Fischer, and W. E. Johns, "Product water mass formation by turbulent density currents from a high-order nonhydrostatic spectral element model," Ocean Modell. **12**, 237–267 (2006).
[24]J. Pelmard, S. Norris, and H. Friedrich, "Statistical characterisation of turbulence for an unsteady gravity current," J. Fluid Mech. **901**, A7 (2020).
[25]C. R. Marshall, R. M. Dorrell, G. M. Keevil, J. Peakall, and S. M. Tobias, "Observations of large-scale coherent structures in gravity currents: Implications for flow dynamics," Exp. Fluids **62**, 120 (2021).
[26]O. E. Sequeiros, "Estimating turbidity current conditions from channel morphology: A Froude number approach," J. Geophys. Res. **117**, C04003, https://doi.org/10.1029/2011JC007201 (2012).
[27]S. B. Pope, *Turbulent Flows* (IOP Publishing, 2001).
[28]M. H. García and J. D. Parsons, "Mixing at the front of gravity currents," Dyn. Atmos. Oceans **24**, 197–205 (1996).
[29]J. D. Parsons and M. H. García, "Similarity of gravity current fronts," Phys. Fluids **10**, 3209–3213 (1998).
[30]S. Balasubramanian and Q. Zhong, "Entrainment and mixing in lock-exchange gravity currents using simultaneous velocity-density measurements," Phys. Fluids **30**, 056601 (2018).
[31]C. A. R. Hogg, S. B. Dalziel, H. E. Huppert, and J. Imberger, "Inclined gravity currents filling basins: The influence of Reynolds number on entrainment into gravity currents," Phys. Fluids **27**, 096602 (2015).
[32]P. L. Miller, "Mixing in high Schmidt number turbulent jets," Ph.D. thesis (California Institute of Technology, 1991).
[33]T. Bonometti and S. Balachandar, "Effect of Schmidt number on the structure and propagation of density currents," Theor. Comput. Fluid Dyn. **22**, 341 (2008).
[34]B. Andersson, R. Andersson, L. Håkansson, M. Mortensen, R. Sudiyo, and B. van Wachem, *Computational Fluid Dynamics for Engineers* (Cambridge University Press, 2011).
[35]D. A. Donzis, K. Aditya, K. R. Sreenivasan, and P. K. Yeung, "The turbulent Schmidt number," J. Fluids Eng. **136**, 060912 (2014).
[36]M. Rahmani, B. R. Seymour, and G. A. Lawrence, "The effect of Prandtl number on mixing in low Reynolds number Kelvin-Helmholtz billows," Phys. Fluids **28**, 054107 (2016).
[37]H. Hanazaki, K. Konishi, and T. Okamura, "Schmidt-number effects on the flow past a sphere moving vertically in a stratified diffusive fluid," Phys. Fluids **21**, 026602 (2009).
[38]J. Langham, T. S. Eaves, and R. R. Kerswell, "Stably stratified exact coherent structures in shear flow: The effect of Prandtl number," J. Fluid Mech. **882**, A10 (2020).
[39]R. B. Bird, W. E. Stewart, and E. N. Lightfoot, *Transport Phenomena*, 2nd ed. (Wiley, 2007).
[40]A. J. Reynolds, *Turbulent Flows in Engineering* (Wiley, 1974).
[41]K. Benes, P. Tong, and B. J. Ackerson, "Sedimentation, Péclet number, and hydrodynamic screening," Phys. Rev. E **76**, 056302 (2007).
[42]V. K. Birman, J. E. Martin, and E. Meiburg, "The non-Boussinesq lock-exchange problem. Part 2. High-resolution simulations," J. Fluid Mech. **537**, 125–144 (2005).
[43]F. Necker, C. Härtel, L. Kleiser, and E. Meiburg, "Mixing and dissipation in particle-driven gravity currents," J. Fluid Mech. **545**, 339 (2005).
[44]C. Härtel, F. Carlsson, and M. Thunblom, "Analysis and direct numerical simulation of the flow at a gravity-current head. Part 2. The lobe-and-cleft instability," J. Fluid Mech. **418**, 213–229 (2000).
[45]S. K. Ooi, G. Constantinescu, and L. J. Weber, "2D large-eddy simulation of lock-exchange gravity current flows at high Grashof numbers," J. Hydraul. Eng. **133**, 1037–1047 (2007).
[46]S. K. Ooi, G. Constantinescu, and L. Weber, "Numerical simulations of lock-exchange compositional gravity current," J. Fluid Mech. **635**, 361 (2009).
[47]D. Deepwell and M. Stastna, "Mass transport by mode-2 internal solitary-like waves," Phys. Fluids **28**, 056606 (2016).
[48]J. Paik, A. Eghbalzadeh, and F. Sotiropoulos, "Three-dimensional unsteady RANS modeling of discontinuous gravity currents in rectangular domains," J. Hydraul. Eng. **135**, 505–521 (2009).
[49]L. F. R. Espath, L. C. Pinto, S. Laizet, and J. H. Silvestrini, "Two- and three-dimensional direct numerical simulation of particle-laden gravity currents," Comput. Geosci. **63**, 9–16 (2014).
[50]L. M. Stancanelli, R. E. Musumeci, and E. Foti, "Computational fluid dynamics for modeling gravity currents in the presence of oscillatory ambient flow," Water **10**, 635 (2018).
[51]J. W. L. Paul, F. Fischer, and S. G. Kerkemeier, see http://nek5000.mcs.anl.gov for "nek5000 Web Page" (2008).
[52]C. R. Marshall, "Experiments and numerical simulation of three-dimensional turbulence in gravity currents," Ph.D. thesis (University of Leeds, 2021).
[53]J. C. McWilliams, *Fundamentals of Geophysical Fluid Dynamics* (Cambridge University Press, 2006).
[54]K. Mittal, S. Dutta, and P. Fischer, "Multirate timestepping for the incompressible Navier-Stokes equations in overlapping grids," J. Comput. Phys. **437**, 110335 (2021).
[55]J. P. Boyd, *Chebyshev and Fourier Spectral Methods*, 2nd ed. (Dover Publications, 2001).
[56]B. Fornberg, *A Practical Guide to Pseudospectral Methods* (Cambridge University Press, 1998).
[57]P. F. Fischer, "An overlapping Schwarz method for spectral element solution of the incompressible Navier–Stokes equations," J. Comput. Phys. **133**, 84–101 (1997).
[58]G. N. Coleman and R. D. Sandberg, "A primer on direct numerical simulation of turbulence - methods, procedures and guidelines," Technical Report No. AFM-09/01a (University of Southampton, 2010).
[59]J. Kim, P. Moin, and R. Moser, "Turbulence statistics in fully developed channel flow at low Reynolds number," J. Fluid Mech. **177**, 133–166 (1987).
[60]M. I. Cantero, S. Balachandar, M. H. García, and J. P. Ferry, "Direct numerical simulations of planar and cylindrical density currents," J. Appl. Mech. **73**, 923–930 (2006).
[61]M. García-Villalba and J. C. del Álamo, "Turbulence modification by stable stratification in channel flow," Phys. Fluids **23**, 045104 (2011).
[62]J. Zhou, R. J. Adrian, S. Balachandar, and T. M. Kendall, "Mechanisms for generating coherent packets of hairpin vortices in channel flow," J. Fluid Mech. **387**, 353–396 (1999).
[63]C. Buckee, B. Kneller, and J. Peakall, "Turbulence structure in steady, solute-driven gravity currents," in *Particulate Gravity Currents*, edited by W. McCaffrey, B. Kneller, and J. Peakall (Wiley, 2001), pp. 173–187.
[64]E. Meiburg and B. Kneller, "Turbidity currents and their deposits," Annu. Rev. Fluid Mech. **42**, 135–156 (2010).
[65]J. E. Simpson and R. E. Britter, "The dynamics of the head of a gravity current advancing over a horizontal surface," J. Fluid Mech. **94**, 477–495 (1979).
[66]B. Kneller, M. M. Nasr-Azadani, S. Radhakrishnan, and E. Meiburg, "Long-range sediment transport in the world's oceans by stably stratified turbidity currents," J. Geophys. Res. **121**, 8608–8620, https://doi.org/10.1002/2016JC011978 (2016).
[67]J. H. Baas, J. L. Best, J. Peakall, and M. Wang, "A phase diagram for turbulent, transitional, and laminar clay suspension flows," J. Sediment. Res. **79**, 162–183 (2009).
[68]J. H. Baas, J. L. Best, and J. Peakall, "Depositional processes, bedform development and hybrid bed formation in rapidly decelerated cohesive (mud–sand) sediment flows," Sedimentology **58**, 1953–1987 (2011).